A Comparative Investigation of Plasmonic Properties between Tunable Nanoobjects and Metallized Nanoprobes for Optical Spectroscopy

Damien Eschimese, Patrick Hsia, Francois Vaurette, D. Deresmes, De Philippe Bettignies, Joachim Schreiber, Marc Chaigneau, S. Arscott, Gaëtan Lévêque, Thierry Melin

A comparative investigation of plasmonic properties between tunable nanoobjects and metallized nanoprobes for optical spectroscopy

Damien ESCHIMÈSE [1,2], Patrick HSIA [2], François VAURETTE [1], Dominique DERESMES [1], Philippe De BETTIGNIES [2], Joachim SCHREIBER [2], Marc CHAIGNEAU [2*], Steve ARSCOTT[1], Gaëtan LÉVÊQUE [1] and Thierry MÉLIN [1*]*

(1) Institute of Electronics Microelectronics and Nanotechnology (IEMN), University of Lille, CNRS UMR 8520, Avenue Poincaré CS 60069, 59652 Villeneuve d'Ascq Cedex, France.

(2) HORIBA France SAS, HORIBA Europe Research Center, Avenue de la Vauve, Passage Jobin Yvon, CS 45002, 91120 Palaiseau, France.

* corresponding author: thierry.melin@iemn.fr

KEYWORDS: plasmonics, dark-field imaging, total-internal-reflection scattering spectroscopy, tip-enhanced optical spectroscopy, atomic force microscopy, nanofabrication, nano-antennas, localized surface plasmons

ABSTRACT

In order to evaluate the optical efficiency of tip-based probes for future tip-enhanced optical spectroscopy applications, we have developed an experimental setup based on the coupling of an achromatic inverted microscope equipped with a total internal reflection objective and an atomic force microscopy (AFM) head. This spectroscopic tool has been validated using individual nanofabricated antennas (gold nanodisks/nanocones) on a glass substrate, which act as nanoresonators based on localized surface plasmons. Spectrally tunable transverse electric and magnetic plasmonic resonances are identified and are in excellent agreement with numerical calculations performed as a function of the nano-antenna geometry and size. We have investigated a series of state-of-the-art gold-coated AFM probes, which are commonly used for tip-enhanced (Raman spectroscopy) optical experiments. Their scattering spectrum consists of resonances depending on the tip sharpness or granularity superimposed on a broad emission spectrum due to semi-infinite metal layer acting as a non-resonant antenna. From the comparison between the plasmonic response of both types of optical antennas, a new generation of probes for tip-enhanced optical spectroscopy is proposed, in which single plasmonic nano-antennas are engineered at the apex of a non-metallic AFM tip. As from numerical simulation results, such tips would ensure a spectral tunability as a function of the material, size, and geometry, together with expected high enhancement factors. Such features would allow the design of spectrally tunable surface enhanced Raman spectroscopy substrates, and should be a reliable and efficient alternative to tips commonly used in tip-enhanced optical spectroscopy experiments such as tip-enhanced Raman spectroscopy.

GRAPHICAL TABLE OF CONTENTS

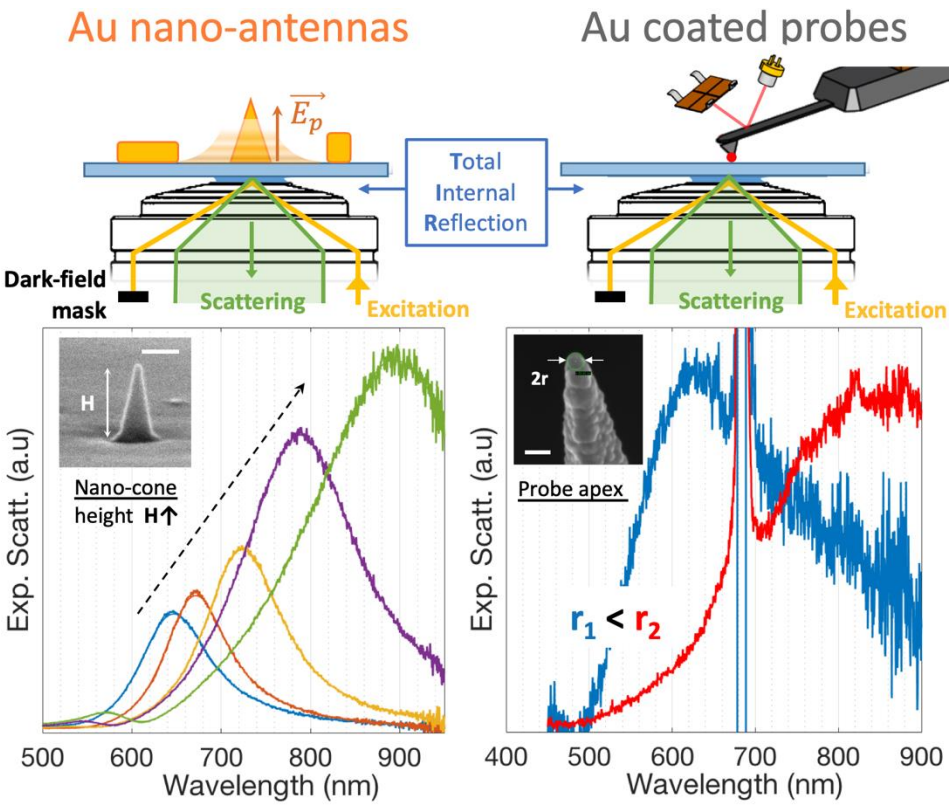

INTRODUCTION

The investigation of optical properties of molecules or individual nanostructures with a spatial resolution less than the diffraction limit requires an electromagnetic field confined at the nanoscale—this can be achieved using adapted optical scanning tip-based probes. This leads, in the case of Raman spectroscopy for example, to the technique referred to as tip-enhanced Raman spectroscopy (TERS)[1–4], which can be used today for correlated chemical and physical surface mapping with nanoscale spatial resolution[5,6]. Scanning probes used for the optical signal amplification benefit in general from plasmonic properties, i.e. sustain propagative and/or localized surface plasmons, whose excitation results in an enhanced optical evanescent field confined in a nanometric volume at the tip apex—referred to as the 'hot-spot'—and governs the tip-enhanced spatial resolution. In the case of Raman spectroscopy, the amplification factor strongly depends on the shape of the tip, and ranges from 10^4 to 10^8 [7,8], enabling TERS mapping with a nanometric resolution[9,10]. Tip-enhanced optical spectroscopy can also be used e.g. to map photoluminescence properties at the nanoscale [11,12].

Focusing here on the case of TERS, a large diversity of plasmonic probes with different designs have been so far discussed in the literature. These include smooth electrochemically etched metallic wires[13–15] commonly used for scanning tunneling microscopy (STM) and granular metallic coatings onto silicon cantilevers commonly used for [16–19] atomic force microscopy (AFM). It has been shown that the roughness of the metallic layer deposited onto probes[20] but also the size of the metallic apex itself[21] have a strong influence on enhancement factors, which vary both in amplitude and as a function of the excitation wavelength. Metal-coated AFM-TERS probes appear simpler to use than STM-TERS probes and allow in principle non-

conductive samples to be investigated. The majority of AFM-TERS probes involve today the use of gold as a metallization layer, mainly for studies in materials sciences. Gold is interesting for its intense plasmonic activity in the visible region but also for its chemical inertness providing long probe lifetimes. However, gold layers only produce plasmonic resonances with wavelengths in the red part of the spectrum, which limits applications e.g. towards the field of semiconductors or biology that require to lower the penetration of the Raman excitation laser in the sample but also to avoid parasitic fluorescence signal. Silver[22,23] and aluminum[24,25] can be used to reach lower wavelengths for such experiments—indeed, the plasmonic activity of silver takes place in the blue-green part of the spectrum, while aluminum can even reach UV[26,27] wavelengths. These materials suffer in practice in terms of sulfidation or oxidation in air, which limits the probe lifetime[28–30]. A reliable control of the spectral response of AFM-based TERS probes, i.e. their spectral tunability, is a still key aspect for TERS experiments and developments.

With the aim of improving the plasmonic response and amplification factors of TERS probes, recent work has started to go beyond metal-coated probes and design the apex of scanning probe microscopy tips[31,32] — for instance by using focused ion beam etching in order to isolate the metallic part that composes the apex from the rest of the metallized tip. This breaks the conventional semi-infinite plasmonic tip model (‘non-resonant‘ tip) by creating an electromagnetic cavity of controlled shape at the tip apex[33], with spectrally well-defined resonances related to the excitation of localized surface plasmon modes (i.e. ‘resonant tips’). In practice, such structured tips as well as granular metallic tips commonly used in TERS experiments may combine non-resonant effects (moderately-enhanced electromagnetic field on the whole white light spectrum) together with resonant effects (presence of spectrally defined

resonances), depending on the tip granularity or apex shape. Moreover, protusion effects have been studied at the theoretical level down to the atomic scale[34,35].

In order to experimentally investigate nano-fabricated probes for tip-enhanced optical spectroscopy applications, in view of controlling their manufacturing process and their spectral tunability, we have developed in this work a spectroscopy tool based on the coupling of an AFM head and an achromatic inverted microscope equipped with a total-internal-reflection (TIR) fluorescence objective. This setup is designed to measure the spectroscopic scattering response of engineered plasmonic nanostructures[36,37] without vacuum constraints such as in electron energy loss spectroscopy[38,39]. The operating principle is close to dark-field scattering[40–43]—but using a TIR illumination[44–49] in order to measure the AFM tip scattering spectrum under scanning conditions, i.e. when an AFM tip is brought into contact with a (transparent) substrate.

This spectroscopic tool has been validated for individual resonant nano-antennas (Au nanodisks or nanocones) on a glass substrate. Spectrally tunable and highly reproducible polarization-dependent plasmonic resonances are identified and are in excellent agreement with numerical calculations performed as a function of the nano-antenna geometry and size. In addition, we investigated a series of state-of-the-art metal-coated AFM tips commonly used for TERS experiments. Their scattering spectrum consists in resonances varying on the tip sharpness or granularity, superimposed on a broad emission spectrum due to semi-infinite metal layer acting as a non-resonant antenna. The comparison between both types of tips is striking, since lithographically-defined nano-antennas exhibit well-defined and spectroscopically tunable plasmonic resonances, while TERS probes based on Au-coated AFM tips only go beyond a non-resonant scattering response only for granular and/or smallest tip apexes. This comparison, together with additional numerical calculations, show that a new generation of AFM-TERS

probes can be envisaged, in which single plasmonic nanofabricated antennas will be localized at the apex of a dielectric AFM tip, ensuring both reproducible and spectrally tunable hot-spots as a function of the plasmonic material, size, and geometry.

EXPERIMENTS AND RESULTS

The spectroscopy tool developed for the study is shown in Figure 1—based on an AFM mounted on an inverted microscope (BioScope, Brüker, Germany). The inverted microscope has been fully rebuilt as shown in Figure 1 using mirror and lenses based on silver-coated mirrors in order to ensure an achromatic behavior over the visible spectrum. The setup is based on a 100x TIR objective (IMMOIL-F30CC, Olympus, Germany) in which a white light source is introduced with a large incidence angle at the TIR objective/glass substrate interface in order to create an evanescent optical field. The TIR objective is used in dark-field mode by blocking the light directly reflected at the objective/glass substrate interface—and only collects the scattered light which is analyzed through a spectrometer (VS7000, HORIBA Scientific, France) equipped with an uncooled CCD detector. This setup enables the acquisition of scattering spectra of single plasmonic structures on a glass substrate within ~100 ms as well as the characterization of individual AFM cantilever tips brought into the evanescent field at the TIR objective/glass substrate interface in tapping or contact mode (see Methods).

We first tested our optical spectroscopy setup on arrays of individual plasmonic nano-antennas consisting either in Au nanodisks or in Au nanocones lithographically-patterned onto a glass substrate—see Figure 2. The structures have been fabricated by evaporation through a PMMA resist-based *lift-off* mask written by electron beam lithography. Because the opening of holes in

the mask is progressively reduced during metal deposition, it is possible to fabricate either Au nanodisks with tilted sides at low metallization thickness (Figure 2a), or Au nanocones, once the holes in PMMA mask are fully closed at a critical metallization thickness (Figure 2b)[50,51]. Nanodisks or nanocones are obtained by choosing the PMMA mask aspect ratio (*resist thickness*/*resist opening width*) and the metallization thickness (see Methods for details).

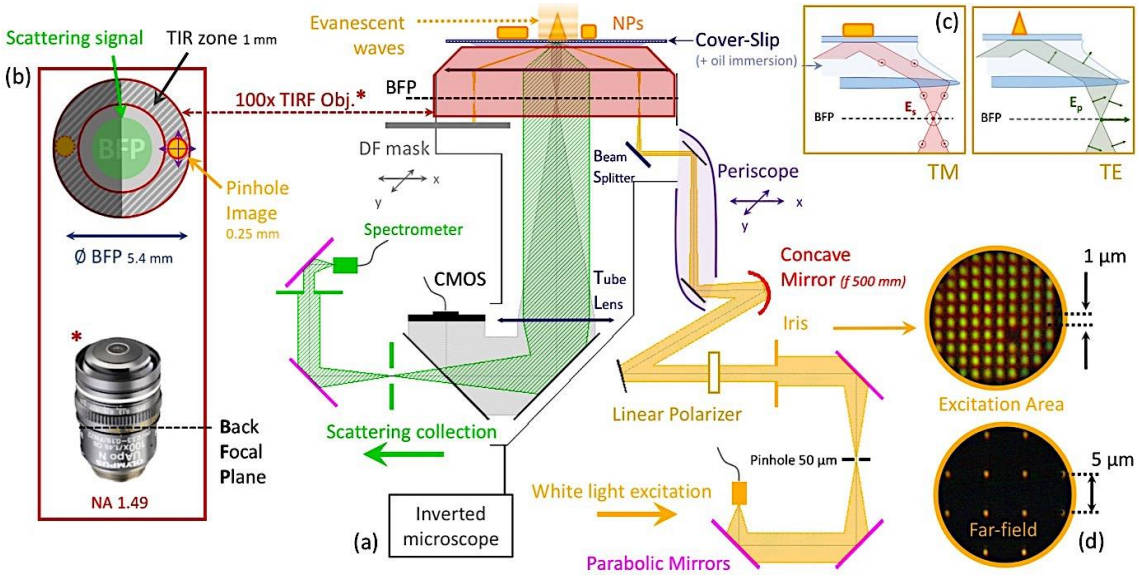

Figure 1: (a) Schematic diagram of the inverted microscope used to measure TIR scattering spectra of nano-resonators fabricated on a glass coverslip (Au nanodisks or nanocones, see Methods) or AFM tips brought into the optical evanescent field at the coverslip/air interface. The AFM head enabling the approach of cantilever tips is not represented here (see Figure 5). Orange optical path: the setup is excited with a white light introduced on the side of the TIR objective back focal plane (see b); the specularly reflected beam is blocked in the objective back focal plane in order to fulfill dark field conditions; a linear polarizer is introduced in the optical path in order to excite nano-antennas either in TE or TM modes (see c). Green optical path: the scattered light is collected via the TIR objective, enabling either the dark-field imaging (see d) or the spectral analysis of the scattered light via a visible spectrometer coupled to a CCD detector. (b) TIR objective with a cross-section in its back-focal plane, showing the incident pinhole image (orange spot), the specular reflection blocked by the dark-field mask, and the collected scattered signal. (c) Schematics of the polarizations used to probe TE and TM modes. (d) Example of acquired far-field images on arrays or metallic nano-antennas lithographically designed on a glass coverslip (1 µm or 5 µm pitch).

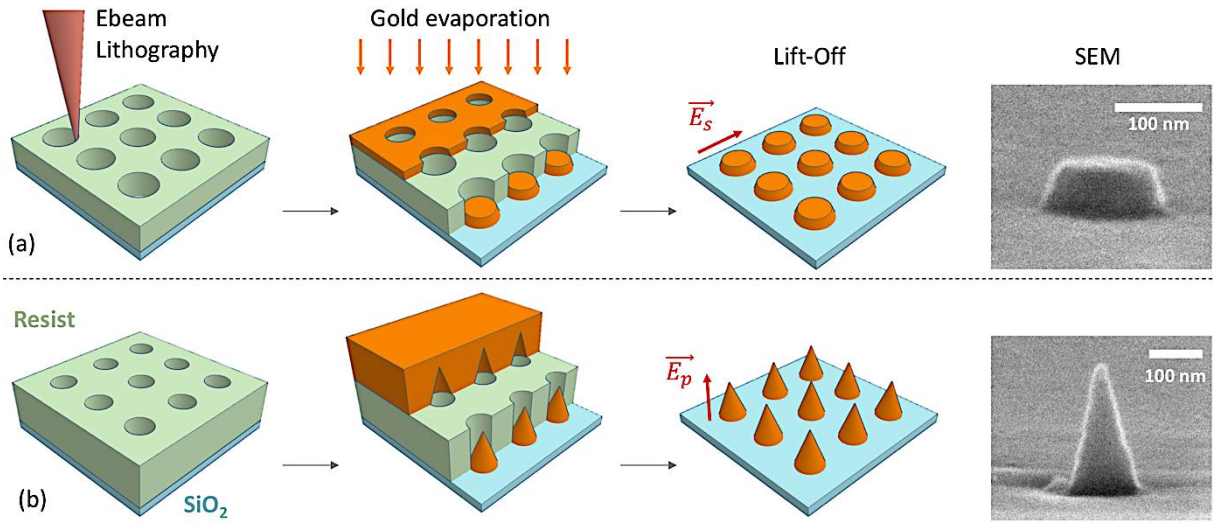

Figure 2: Fabrication sequence for (a) Au nanodisks and (b) Au nanocones. Left: schematic diagram of the fabrication process, in which a PMMA resist layer is exposed by electron beam lithography; Au is then evaporated through the obtained mask, followed by a lift-off process leading either to nanodisks or nanocones at large evaporation thickness. Right: corresponding scanning electron micrographs for Au nanodisks of nanocones.

We start with a series of Au nanodisks fabricated on a glass substrate, with a thickness of about 50 nm and diameters in the 100-160 nm range. Both transverse electric (TE, incident electric field parallel to the substrate) and transverse magnetic (TM, incident magnetic field parallel to the substrate) linear polarizations (see Figure 1c) have been probed under TIR conditions and are hereafter labelled TIR-TE and TIR-TM. For each single nano-antenna, we have recorded the associated TIR scattering spectrum in the 400-900 nm wavelength range. Background noise (recorded on the glass substrate) has been subtracted from experimental TIR spectra, and a normalization by the reference spectrum of the excitation white light (measured by collecting the incident directly reflected at the glass/air interface, without mask) has been applied. For sake of comparison with experiments, theoretical scattering spectra have been computed

together with three-dimensional representations of the far-field radiation for each TE or TM polarization, using finite element simulations (COMSOL software, see Methods).

Experimentally-obtained and theoretically-computed data are shown in Figure 3a and 3b to allow a comparison. We observe in the TIR-TE polarization a single resonance, which exhibits a redshift for increasing Au nanodisks diameters. This mode corresponds to a plasmon associated with a horizontal dipole (H_D, see illustration in Figure 3b), for which a spectral redshift with larger diameters is predicted by the plasmon theory and is linked to the lowering of the restoring force exerted on free electrons at the surface of the particle[52]. The experimental data are in excellent agreement with theoretical scattering spectra. Experimental far-field images (see Figure 3c) also show similarities with the calculated radiation patterns. However, the situation is more complex for the TIR-TM polarization. Experimental scattering spectra (Figure 3d) exhibit two resonances—these are well accounted for by numerical modelling (Figure 3d). The resonance at larger wavelength corresponds to the same horizontal dipolar mode as in the TIR-TE polarization and exhibits the same redshift with increasing nanodisk diameter. This reminiscence of the H_D mode is due to the tilt angle of the optical excitation in the TIR objective (see schematic diagram of the TIR-TE and TIR-TM polarizations in Figure 1). In contrast, the shorter-wavelength resonance is almost insensitive to the nanodisk diameter. This resonance is well accounted for in numerical calculations and corresponds to a vertical dipolar (V_D) mode[53] (see inset of Figure 3e for an illustration). The experimental evolution of the wavelength and amplitude of the two resonances as a function of the nanodisk diameter is accurately predicted by numerical modeling, taking the incidence angle of the illumination equal to 44°. The calculated far-field radiation patterns of the V_D mode, shown in Figure 3f, presents a typical ‘donut’ shape radiation pattern, observed in the experiments, and which is due to the cancellation of far-field radiation in the direction of the induced dipole.

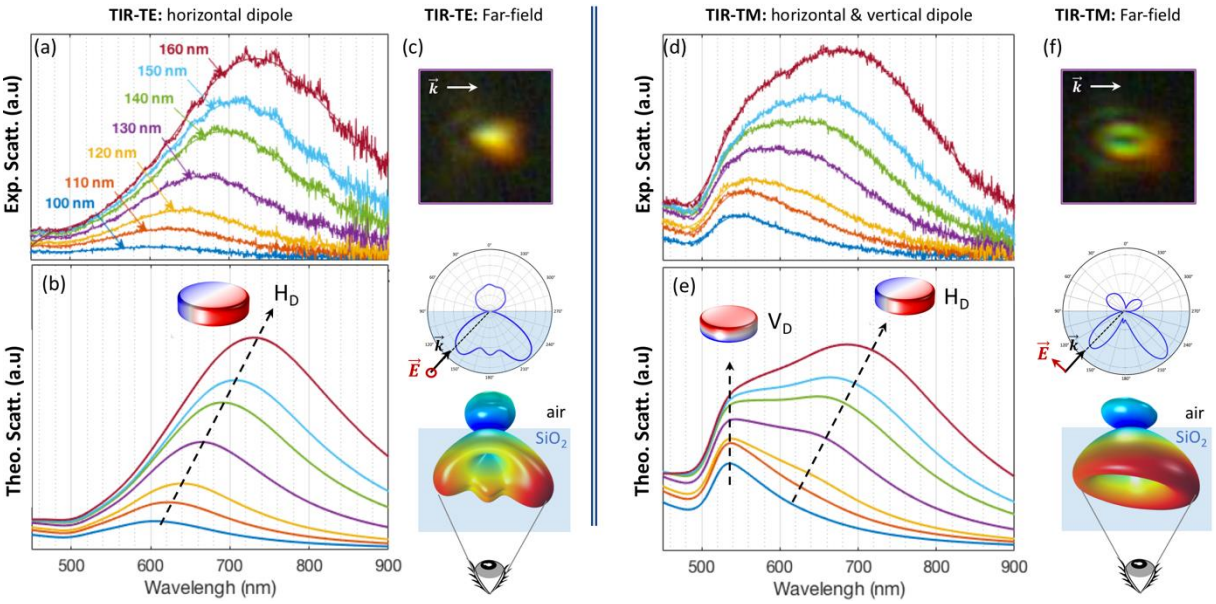

Figure 3: (a) Experimental TIR-TE scattering spectra for a series of individual Au nanodisks as a function of their base diameter (colors are used in the rest of the figure to label for the nanodisks diameters). (b) Corresponding calculated TIR-TE spectra, showing a horizontal dipole (H_D) resonance sketched in the inset. (c) Far-field image of a single Au nanodisk (top) of 130 nm diameter, and radiation patterns of the H_D mode in the plane normal to the air/glass interface (middle), and in a three-dimensional representation (bottom). (d) Experimental TIR-TM spectra for the same series of Au nanodisks. (e) Corresponding calculated TIR-TM spectra, showing a resurgence of the H_D mode at larger wavelength (see the black-dashed arrow as a guide to the eye) due to the tilt angle of the incident light, and a second resonance at lower wavelength, corresponding to a vertical dipole (V_D) mode, mostly insensitive to the nanodisk diameter. The insets show schematics of the two dipolar modes. (f) Calculated radiation patterns associated with the V_D mode (bottom) showing a donut-like shape, together with an experimental far-field image of the same Au nanodisk used in (c).

The next part of the study focuses on characterization and modeling of individual gold nanocones with heights in the 105-250 nm range and a cone half-angle of about 12.5°. Under TIR-TM illumination, such structures exhibit intense plasmon resonances with vertical dipole character due to their large vertical aspect ratio. Far-field optical images and experimental scattering spectra are shown in Figure 4, together with numerical calculations. The dimensions of the Au nanocones (height H, half-angle θ, and apex radius r) have been measured individually

from scanning electron microscopy images (see Methods). The dimensions used in the numerical model fit the experimentally obtained dimensions to an accuracy within a few percent (see data are provided in Supporting Information, Table SI- 1). TIR-TM scattering spectra and numerical calculations both reveal a dipolar and a higher-order vertical plasmonic mode, as shown in the inset of Figure 4. The first series of nanocones (NC1 to NC5), with heights ranging from 105 to 205 nm, exhibits a pronounced dipolar resonance in the visible range (550-800 nm) except for NC5. In the latter case, both experimental and theoretical results show the emergence of a higher order mode in the green region, of quadrupole type, since the dipolar resonance falls in the infrared. For larger nanocones (here, labeled from NC6 to NC9, with heights from 195 to 245 nm), the quadrupolar plasmon resonance dominates in the 500-650 nm wavelength range. As in the case of the Au nanodisks, the evolution of experimental TIR spectra are consistent with the numerical analysis conducted as a function of the Au nanocone dimensions.

Figure 4: Experimental TIR scattering spectra recorded (top) and calculated (bottom) for a TM optical

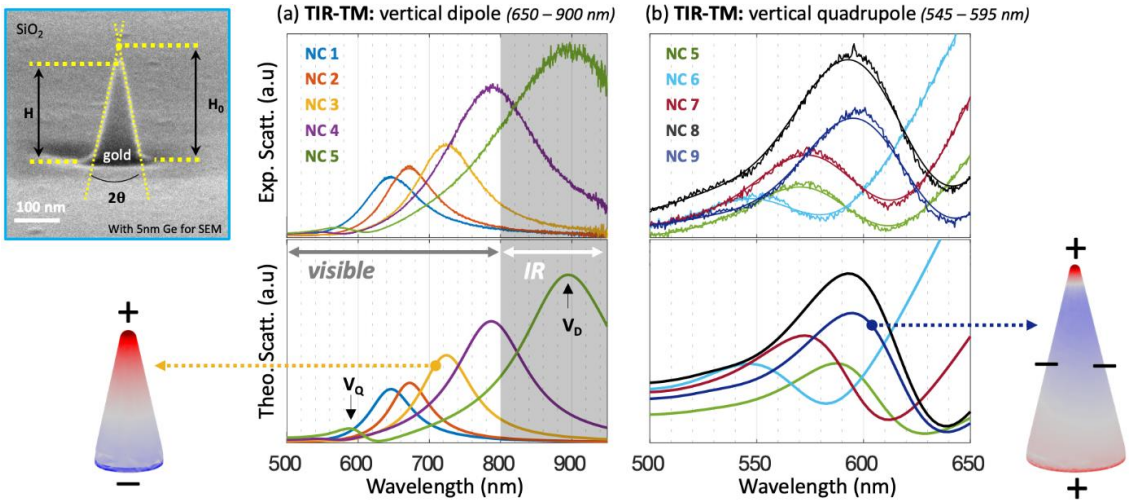

excitation. Data for nanocones NC1-NC5 are shown in (a) and exhibit dipole resonances in the 500 nm-900 nm wavelength range. Data for larger nanocones NC6-NC9 are shown in (b) and exhibit quadrupole resonances in the 500 nm – 650 nm wavelength range (see text). Insets show a typical scanning electron micrograph of the nanocone geometry, and 3D numerical representations of surface charges to illustrate the dipole and quadrupole plasmon resonances.

Altogether, the results obtained both on Au nanodisks and nanocones show the relevance of our TIR scattering spectroscopy setup to capture the plasmonic properties of nano-resonators as a function of their size and geometry. They also promote the ability of finite element calculations used in this work to quantitatively account for the detailed optical properties of individual metallic nano-resonators as a function of their geometry.

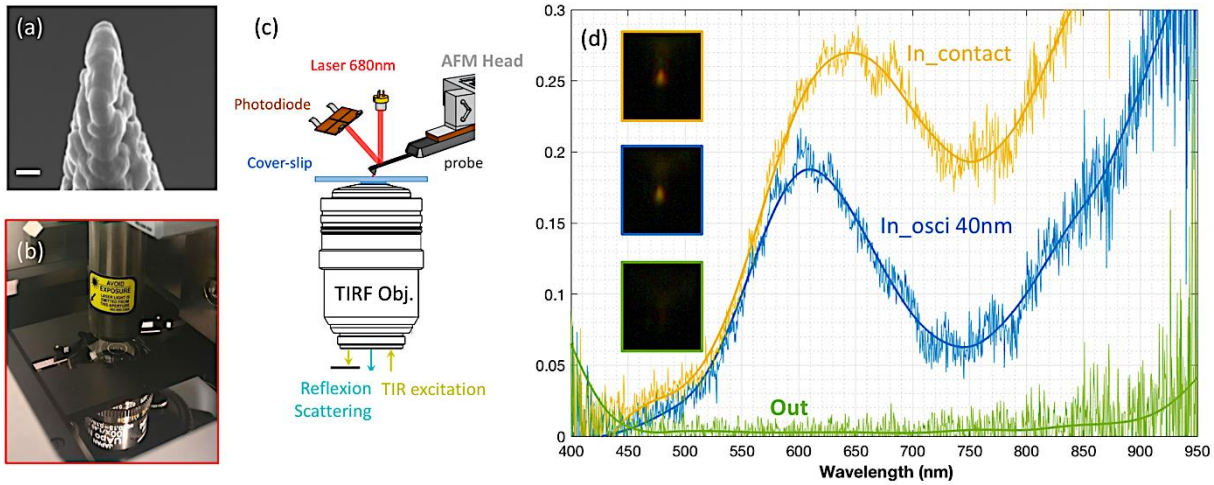

Figure 5: (a) Scanning electron micrograph of the apex of the AFM-TERS cantilever-based tip (here, a Au-coated cantilever with 40 nm apex radius – scale bar 100nm). (b) The cantilever is mounted on the AFM head located above the TIR microscope. (c) Schematics of the measurement configuration, in which the TERS tip is brought in the evanescent field of a glass coverslip above the TIR objective using the regulation of the AFM head. (d) TIR scattering spectra for the Au-coated tip shown in (a). The green, blue, and orange curves are the normalized TIR scattering spectra recorded respectively with the tip located 200 nm above the glass coverslip, with the tip engaged on the surface in tapping-mode with a 40 nm oscillation amplitude, and with the tip engaged in contact mode. Far-field optical images are shown as insets.

We also characterized individual cantilever-based AFM-TERS probes fabricated by metal evaporation on standard commercial AFM tips (ACCESS-NC probes, Applied NanoStructures, Inc., USA). We describe in the following the acquisition of TIR spectra on the example of a

Au-coated tip, and then compare TIR scattering spectra for a set of three Au-coated probes. Cantilevers based probes (see Figure 5a) are brought into the evanescent optical field of the TIR objective covered with a glass substrate using the AFM head of the original AFM setup covering our TIR imaging setup (see Figure 5b and 5c). AFM-TERS probes are first engaged in tapping mode on the glass substrate above the center of the TIR objective. The position of the tip is finely adjusted in a second step, using the AFM head horizontal piezoelectric displacements, in order to bring the tip to the center of the optical excitation spot. The acquired TIR spectra are subtracted from the optical setup background noise, which is recorded as a reference in absence of any tip, and then normalized with respect to the excitation light spectrum. The TIR spectra for an Au-coated AFM-TERS probe is presented in Figure 5c. The green curve corresponds to the TIR spectrum acquired with the TERS probes retracted to ~200 nm away from the substrate surface, and exhibits almost no response—as would be expected for a probe out of the evanescent optical field from the substrate. The increased noise level at the edges of the recorded spectrum is due to the cut-off of the optical setup (mainly, of the TIR objective) out of the visible range, which reduces the amount of light detected at such wavelengths. A TIR scattering spectrum of the TERS tip is first shown (blue curve in Figure 5c) when the tip is engaged on the surface in tapping mode (average oscillation amplitude of ~40 nm); also corresponding to a bright spot in the dark-field image (see insets in Figure 5c). The TIR scattering spectrum shows a well-defined resonance at a wavelength of about 600 nm, while a background develops at larger wavelengths (> 800 nm). When the tip approaches the surface by switching the AFM regulation from tapping mode to contact mode (orange curve in Figure 5c), the TIR spectrum shows an enhanced signal and preserved structure, with an observable redshift of the resonance now occurring at a wavelength of ~650 nm. This redshift

in the scattering spectrum can be explained by the interaction of the dipolar localized plasmon mode supported by the tip and its image in the glass substrate[54].

We also performed a comparison between a set of three Au-coated AFM-TERS probes (see Figure 6) using the same protocol as in the experiments shown in Figure 5. Probes appear almost identical in individual SEM images (see Figure 6a). They exhibit a tip apex radius of curvature between ~35 nm and ~45 nm — this radius mainly depends on the metal coating local roughness at the tip apex. TIR scattering spectra are shown in Figure 6b. The systematic sharp peak observed at a wavelength of 685 nm corresponds to a parasitic detection of the AFM head laser and needs to be disregarded. The probes present a 'white' scattering background response (see Figure 6b), which is typical of a semi-infinite metallic (non-resonant) antenna. In addition, the scattering spectra also show a plasmon resonance around 630 nm and 850 nm for the tips with radius of curvature about 35nm and 40 nm respectively. For a larger radius of curvature (45 nm), the main resonance reaches the infrared region. We thus observe as a trend that sharper tips produce localized surface plasmon resonances with high oscillator strength and occur at shorter wavelengths. This spectral dependence related to the variation of the probe radii of curvature of only 5 nm (most certainly due to the roughness at the tip vicinity) is strong and appears difficult to control during the thermal evaporation of the gold layer on the AFM tip.

When put in the general context of tip-enhanced optical spectroscopy measurements, the work presented in this study shows that an important difference exists between metallic nanostructures fabricated by nanolithography (e.g. the nanodisks or nanocones presented and measured here) and the AFM based probes commonly used in TERS experiments (here, metal-coated tips). It is striking that the former nanostructures reproducibly give rise to clear-cut

localized surface plasmon resonances with a tunable and controllable wavelength, while the latter tips show a variability of localized surface plasmon resonance wavelength from tip to tip. One reason for such a difference is that the localized surface plasmon resonance of metal-plated probes is related to specific tip apex radius size and/or granularity and thus strongly size dependent, while the wavelength of the LSPR of individual metallic nanostructures is controlled by a *mesoscopic* size parameter such as their height in the case of nanocones of the Figure 4. Nanocones exhibit additionally a reproducible apex radius of 9.9 ± 1.3 nm (the error bar corresponds to the standard deviation for a series of 168 nanocones), contributing to a narrowing of the electromagnetic field lines at the tip apex[55] as required for intense field enhancement required for TERS experiments[56,57]. We therefore suggest that a new generation of AFM-TERS probes based on single nanostructures (such as the nanodisks or nanocones lithographically patterned at the apex of a cantilever) and engineered with a specific design or geometry according to an optimized numerical modelling. Such cantilevers should exhibit localized surface plasmon resonances with tunable wavelength and adjustable enhancement factors (e.g. from the control of the plasmonic dipolar resonance), and are expected —at least in principle— to offer superior performances compared to current metal-coated AFM-TERS probes.

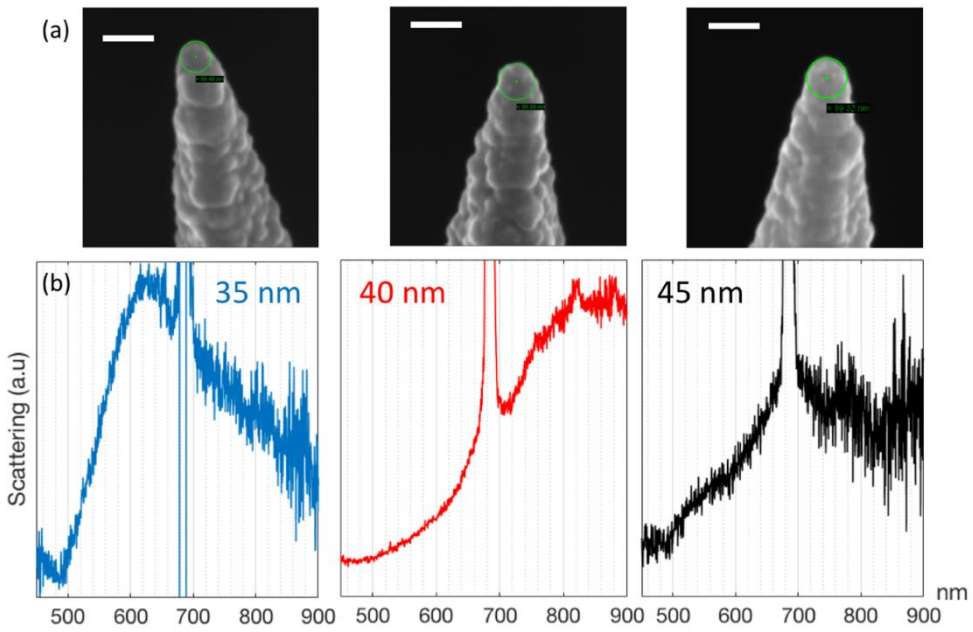

Figure 6: (a) Scanning electron micrograph provided for a set of three commercial Au-coated AFM tips. The scale bar is 100 nm. Apex radii are highlighted. (b) Corresponding TIR scattering spectra. The tip apex radii are shown in insets. The line or discontinuity at 685 nm corresponds to a parasitic detection of the laser line of the AFM head and should be disregarded.

To support our statement, we present in the Supporting Information a numerical study based on the metal nanocone ending a dielectric tip, which shows the advantages of using a dielectric/metal hybrid tip with different sizes of the metallic apex rather than a full metallic bulk system in terms of plasmon resonance tunability and enhancement factor (Figure SI-2). Those results clearly indicate that such tips clearly should surpass, as from the numerical predictions of their electromagnetic enhancement factors, the performances of full metal tips (made either of Au or Ag) used e.g. in TERS experiments.

CONCLUSION

In conclusion, we have developed an experimental spectroscopic setup based on the coupling of atomic force microscopy (AFM) and an achromatic inverted microscope equipped with a

total internal reflection fluorescence objective. TIR scattering spectra of individual nanolithographically fabricated nano-antennas (Au nanodisks or nanocones) show clear and spectrally-tunable resonances associated with local surface plasmons and are in excellent agreement with numerical modeling. In contrast, the scattering spectra of Au-coated cantilever-based AFM probes commonly used for TERS experiments show local surface plasmon resonances related to the tip sharpness and/or granularity superimposed on a 'white' background signal, with a tip-to-tip spectral variability. The comparison between both types of optical antennas suggests that a new generation of AFM-TERS probes is on the horizon, in which single plasmonic nano-antenna are engineered onto the apex of non-metallic AFM tips. Such tips should ensure high field enhancement factors together with a controllable spectral tunability as a function of the plasmonic material, size, and geometry.

METHODS

***Coupled optical and atomic force microscopy setup*.** The device setup shown in Figure 1 is based on an inverted microscope (Olympus IX71, Germany) equipped with a high numerical aperture objective (NA 1.49 - UAPON 1000XOTIRF – Olympus). A broadband white light source (LDLS EQ-99XFC, ENERGETIQ, US) is used as an intense and unpolarized excitation light. To avoid chromatic aberrations, silver coated parabolic, concave and plane mirrors are used in the setup. The incident light from the fiber is firstly collimated and focused into a 50 µm pinhole before being collimated again to cross an iris and a linear polarizer—three parabolic mirrors are involved here. The filtered and polarized pinhole point source is then reflected by a long-focal concave mirror and enters the microscope through a periscope. The light is reflected onto a beam splitter and finally focused on one side of the TIR objective back focal plane to

allow total internal reflection excitation at the cover slip/air interface. The focal image of the pinhole source has a size of about a quarter of millimeter and can be finely positioned in the TIR objective back focal plane using XY micrometric screws (see Figure 1b). The incident beam gets reflected on the glass-air interface under TIR conditions, goes back into the objective and is blocked by a mask on the other half of the TIR objective back focal plane. This mask can also be finely positioned in the TIR objective back focal plane using XY micrometric screws. The substrate thickness is in the 150-200 µm range (Schott D 263® M cover glass). An immersion oil (IMMOIL-F30CC, Olympus, Germany) is used to ensure the lens-substrate contact. The first tunable iris allows us to control the excitation spot on the substrate interface. The light scattered in the evanescent field at the coverslip/air interface is collected in the center of the TIR objective, goes through the beam splitter and is focused by the tube lens of the microscope onto a CCD camera to obtain scattered far-field imaging. To acquire TIR spectra, the scattered light is focused on a second tunable iris in order to control the collection area on the substrate interface with a spatial magnification of 0.01. It is then collimated and focused onto the entrance slit of the spectrometer (VS7000 – HORIBA Scientific, France) equipped with an uncooled CMOS camera. For an incident light source spectral power density between 40 and 85 µW/nm in the visible range, this setup performs the scattering spectrum analysis of single gold nano-antennas with a ~100 ms acquisition time and a large signal-noise ratio.

Numerical modelling. In order to compare experimental results with theory, we performed finite element simulations with the radiofrequency module of COMSOL Multiphysics. Dielectric parameters of gold used for the calculation have been extracted by interpolation of Johnson and Christy's data[58]. To model our experimental configuration, nanoparticles or tips have been placed on or close to a glass substrate with refractive index 1.5. The excitation field

is the combination of the incident (with an angle larger than the critical angle of 41.8°), the reflected planewave propagating in glass, and the evanescent wave transmitted along the interface in air. The outer layer of the computation domain is set as a perfectly matched layer where all the outgoing scattered waves are absorbed, in order to prevent unwanted reflection onto boundaries.

Nanofabrication. Electron beam lithography (Raith EBPG 500 Plus at 100kV) and thermal evaporation have been used to create arrays of gold nanostructures[50,51]. A bi-layer positive resist is deposited on the glass substrate by spin coating, followed by a deposition of a 5 nm thick layer of Ge to prevent charging effect from the electron beam (400 μC cm^{-2} dose, 12 nA beam current). After the writing process, the Ge layer is removed (H_2O_2/H_2O: vol/vol = 1/1) before the resist development. Following resist development, thermal evaporation of gold is performed onto the wafer and metallic nanostructures are obtained via lift-off (using a commercial resist remover at 70°C). The key parameter to fabricate nano-disks or nano-cones are the aspect ratio of exposed cylindrical patterns and the amount of evaporated metal. To create nano-disks, only 50 nm of Au is evaporated onto a 200 nm thick resist layer, with hole diameters between 100 and 200 nm. The evaporation tends to close the hole apertures, accounting for the observed tilted edges of the fabricated nanodisks (see Figure 2a). For conical structures, 250 nm of Au is evaporated on a 500 nm thick resist layer with hole diameters between 50 and 100 nm. In this case, the holes in the PMMA layer become fully closed during the evaporation process (see Figure 2b). The Au nanocones exhibit cone half-angles of ~12°, a height ranging from 100 to 230 nm (which depends on the hole diameter of the patterns), and apex radii falling below 10 nm. All structures have been fabricated in arrays with a 10 μm pitch on the glass substrate to allow an easy access to individual structures in optical measurements.

AUTHOR INFORMATION

Corresponding Author

* thierry.melin@iemn.fr

Author Contributions

The manuscript was written through contributions of all authors. All authors have given approval to the final version of the manuscript.

ACKNOWLEDGMENT

We acknowledge fruitful discussions with P. Tilmant, C. Ha and O. Kérivel. This work has been performed by using the facilities of the French RENATECH network and of the ExCELSiOR Nanoscience Characterization Center. We acknowledge financial support from the French Région Hauts de France under contracts DOS0025370/00 and 17007720, and from the National Research Agency (ANR) under contract ANR-16-CE09-0029. D. Eschimèse acknowledges financial support from the ANRT via a CIFRE grant N°2015/0803.

ABBREVIATIONS

Tip-Enhanced Raman Spectroscopy (TERS); Atomic Force Microscopy (AFM); Transverse Electric (TE); Transverse Magnetic (TM); Total Internal Reflection (TIR).

REFERENCES

(1) Anderson, M. S. Locally Enhanced Raman Spectroscopy with an Atomic Force Microscope. *Appl. Phys. Lett.* **2000**, *76* (21), 3130–3132. https://doi.org/10.1063/1.126546.

(2) Hayazawa, N.; Inouye, Y.; Sekkat, Z.; Kawata, S. Metallized Tip Amplification of Near-Field Raman Scattering. *Opt. Commun.* **2000**, *183* (1–4), 333–336. https://doi.org/10.1016/S0030-4018(00)00894-4.

(3) Stöckle, R. M.; Suh, Y. D.; Deckert, V.; Zenobi, R. Nanoscale Chemical Analysis by Tip-Enhanced Raman Spectroscopy. *Chem. Phys. Lett.* **2000**, *318* (1–3), 131–136. https://doi.org/10.1016/S0009-2614(99)01451-7.

(4) Pettinger, B.; Ren, B.; Picardi, G.; Schuster, R.; Ertl, G. Nanoscale Probing of Adsorbed Species by Tip-Enhanced Raman Spectroscopy. *Phys. Rev. Lett.* **2004**, *92* (9). https://doi.org/10.1103/PhysRevLett.92.096101.

(5) Su, W.; Kumar, N.; Krayev, A.; Chaigneau, M. In Situ Topographical Chemical and Electrical Imaging of Carboxyl Graphene Oxide at the Nanoscale. *Nat. Commun.* **2018**, *9* (1). https://doi.org/10.1038/s41467-018-05307-0.

(6) Smithe, K. K. H.; Krayev, A. V.; Bailey, C. S.; Lee, H. R.; Yalon, E.; Aslan, O. B.; Munoz Rojo, M.; Krylyuk, S.; Taheri, P.; Davydov, A. V.; et al. Nanoscale Heterogeneities in Monolayer MoSe $_2$ Revealed by Correlated Scanning Probe Microscopy and Tip-Enhanced Raman Spectroscopy. *ACS Appl. Nano Mater.* **2018**, *1* (2), 572–579. https://doi.org/10.1021/acsanm.7b00083.

(7) Pettinger, B.; Schambach, P.; Villagómez, C. J.; Scott, N. Tip-Enhanced Raman Spectroscopy: Near-Fields Acting on a Few Molecules. *Annu. Rev. Phys. Chem.* **2012**, *63* (1), 379–399. https://doi.org/10.1146/annurev-physchem-032511-143807.

(8) Milekhin, A. G.; Rahaman, M.; Rodyakina, E. E.; Latyshev, A. V.; Dzhagan, V. M.; Zahn, D. R. T. Giant Gap-Plasmon Tip-Enhanced Raman Scattering of MoS $_2$ Monolayers on Au Nanocluster Arrays. *Nanoscale* **2018**, *10* (6), 2755–2763. https://doi.org/10.1039/C7NR06640F.

(9) Kumar, N.; Mignuzzi, S.; Su, W.; Roy, D. Tip-Enhanced Raman Spectroscopy: Principles and Applications. *EPJ Tech. Instrum.* **2015**, *2* (1). https://doi.org/10.1140/epjti/s40485-015-0019-5.

(10) Wickramasinghe, H. K.; Chaigneau, M.; Yasukuni, R.; Picardi, G.; Ossikovski, R. Billion-Fold Increase in Tip-Enhanced Raman Signal. *ACS Nano* **2014**, *8* (4), 3421–3426. https://doi.org/10.1021/nn406263m.

(11) Okuno, Y.; Lancry, O.; Tempez, A.; Cairone, C.; Bosi, M.; Fabbri, F.; Chaigneau, M. Probing the Nanoscale Light Emission Properties of CVD-Grown MoS2 Monolayer by Tip-Enhanced Photoluminescence. *Nanoscale* **2018**, 14055.

(12) Kumar, N.; Zoladek-Lemanczyk, A.; Guilbert, A. A. Y.; Su, W.; Tuladhar, S. M.; Kirchartz, T.; Schroeder, B. C.; McCulloch, I.; Nelson, J.; Roy, D.; et al. Simultaneous Topographical, Electrical and Optical Microscopy of Optoelectronic Devices at the Nanoscale. *Nanoscale* **2017**, *9* (8), 2723–2731. https://doi.org/10.1039/C6NR09057E.

(13) Kharintsev, S.; Alekseev, A.; Loos, J. Etchant-Based Design of Gold Tip Apexes for Plasmon-Enhanced Raman Spectromicroscopy. *Spectrochim. Acta. A. Mol. Biomol. Spectrosc.* **2017**, *171*, 139–143. https://doi.org/10.1016/j.saa.2016.07.048.

(14) Lopes, M.; Toury, T.; de La Chapelle, M. L.; Bonaccorso, F.; Giuseppe Gucciardi, P. Fast and Reliable Fabrication of Gold Tips with Sub-50 Nm Radius of Curvature for Tip-Enhanced Raman Spectroscopy. *Rev. Sci. Instrum.* **2013**, *84* (7), 073702. https://doi.org/10.1063/1.4812365.

(15) Ren, B.; Picardi, G.; Pettinger, B. Preparation of Gold Tips Suitable for Tip-Enhanced Raman Spectroscopy and Light Emission by Electrochemical Etching. *Rev. Sci. Instrum.* **2004**, *75* (4), 837–841. https://doi.org/10.1063/1.1688442.

(16) Yang, L.-K.; Huang, T.-X.; Zeng, Z.-C.; Li, M.-H.; Wang, X.; Yang, F.-Z.; Ren, B. Rational Fabrication of a Gold-Coated AFM TERS Tip by Pulsed Electrodeposition. *Nanoscale* **2015**, *7* (43), 18225–18231. https://doi.org/10.1039/C5NR04263A.

(17) Brejna, P. R.; Griffiths, P. R. Electroless Deposition of Silver onto Silicon as a Method of Preparation of Reproducible Surface-Enhanced Raman Spectroscopy Substrates and Tip-Enhanced Raman Spectroscopy Tips. *Appl. Spectrosc.* **2010**, *64* (5), 493–499. https://doi.org/10.1366/000370210791211682.

(18) Sanders, A.; Zhang, L.; Bowman, R. W.; Herrmann, L. O.; Baumberg, J. J. Facile Fabrication of Spherical Nanoparticle-Tipped AFM Probes for Plasmonic Applications. *Part. Part. Syst. Charact.* **2015**, *32* (2), 182–187. https://doi.org/10.1002/ppsc.201400104.

(19) Trautmann, S.; Richard-Lacroix, M.; Dathe, A.; Schneidewind, H.; Dellith, J.; Fritzsche, W.; Deckert, V. Plasmon Response Evaluation Based on Image-Derived Arbitrary Nanostructures. *Nanoscale* **2018**, *10* (21), 9830–9839. https://doi.org/10.1039/C8NR02783H.

(20) Taguchi, A.; Yu, J.; Verma, P.; Kawata, S. Optical Antennas with Multiple Plasmonic Nanoparticles for Tip-Enhanced Raman Microscopy. *Nanoscale* **2015**, *7* (41), 17424–17433. https://doi.org/10.1039/C5NR05022G.

(21) Maouli, I.; Taguchi, A.; Saito, Y.; Kawata, S.; Verma, P. Optical Antennas for Tunable Enhancement in Tip-Enhanced Raman Spectroscopy Imaging. *Appl. Phys. Express* **2015**, *8* (3), 032401. https://doi.org/10.7567/APEX.8.032401.

(22) Rasmussen, A.; Budich, C.; Deckert, V. Tip-Enhanced Raman Scattering of a DNA Binding Compound; Mahadevan-Jansen, A., Petrich, W. H., Eds.; San Jose, CA, 2006; p 60930Z. https://doi.org/10.1117/12.646274.

(23) Yeo, B.-S.; Zhang, W.; Vannier, C.; Zenobi, R. Enhancement of Raman Signals with Silver-Coated Tips. *Appl. Spectrosc.* **2006**, *60* (10), 1142–1147. https://doi.org/10.1366/000370206778664662.

(24) Poborchii, V.; Tada, T.; Kanayama, T.; Geshev, P. Optimization of Tip Material and Shape for Near-UV TERS in Si Structures. *J. Raman Spectrosc.* **2009**, *40* (10), 1377–1385. https://doi.org/10.1002/jrs.2417.

(25) Lipiec, E.; Japaridze, A.; Szczerbiński, J.; Dietler, G.; Zenobi, R. Preparation of Well-Defined DNA Samples for Reproducible Nanospectroscopic Measurements. *Small* **2016**, *12* (35), 4821–4829. https://doi.org/10.1002/smll.201601711.

(26) Park, K.-D.; Kim, Y. H.; Park, J.-H.; Park, J. S.; Lee, H. S.; Yim, S.-Y.; Lee, Y. H.; Jeong, M. S. Ultraviolet Tip-Enhanced Nanoscale Raman Imaging: Ultraviolet Tip-Enhanced Nanoscale Raman Imaging. *J. Raman Spectrosc.* **2012**, *43* (12), 1931–1934. https://doi.org/10.1002/jrs.4158.

(27) Yang, Z.; Li, Q.; Fang, Y.; Sun, M. Deep Ultraviolet Tip-Enhanced Raman Scattering. *Chem. Commun.* **2011**, *47* (32), 9131. https://doi.org/10.1039/c1cc13291a.

(28) Opilik, L.; Dogan, U.; Szczerbiński, J.; Zenobi, R. Degradation of Silver Near-Field Optical Probes and Its Electrochemical Reversal. *Appl. Phys. Lett.* **2015**, *107* (9), 091109. https://doi.org/10.1063/1.4929880.

(29) Opilik, L.; Dogan, U.; Li, C.-Y.; Stephanidis, B.; Li, J.-F.; Zenobi, R. Chemical Production of Thin Protective Coatings on Optical Nanotips for Tip-Enhanced Raman

Spectroscopy. *J. Phys. Chem. C* **2016**, *120* (37), 20828–20832. https://doi.org/10.1021/acs.jpcc.6b02147.

(30) Barrios, C. A.; Malkovskiy, A. V.; Hartschuh, R. D.; Kisliuk, A. M.; Sokolov, A. P.; Foster, M. D. Extending Lifetime of Plasmonic Silver Structures Designed for High-Resolution Chemical Imaging or Chemical and Biological Sensing; Fountain III, A. W., Gardner, P. J., Eds.; Orlando, FL, 2008; p 69540C. https://doi.org/10.1117/12.777304.

(31) Vasconcelos, T. L.; Archanjo, B. S.; Fragneaud, B.; Oliveira, B. S.; Riikonen, J.; Li, C.; Ribeiro, D. S.; Rabelo, C.; Rodrigues, W. N.; Jorio, A.; et al. Tuning Localized Surface Plasmon Resonance in Scanning Near-Field Optical Microscopy Probes. *ACS Nano* **2015**, *9* (6), 6297–6304. https://doi.org/10.1021/acsnano.5b01794.

(32) Archanjo, B. S.; Vasconcelos, T. L.; Oliveira, B. S.; Song, C.; Allen, F. I.; Achete, C. A.; Ercius, P. Plasmon 3D Electron Tomography and Local Electric-Field Enhancement of Engineered Plasmonic Nano-Antennas. *ACS Photonics* **2018**. https://doi.org/10.1021/acsphotonics.8b00125.

(33) Novotny, L. Effective Wavelength Scaling for Optical Antennas. *Phys. Rev. Lett.* **2007**, *98* (26). https://doi.org/10.1103/PhysRevLett.98.266802.

(34) Barbry, M.; Koval, P.; Marchesin, F.; Esteban, R.; Borisov, A. G.; Aizpurua, J.; Sánchez-Portal, D. Atomistic Near-Field Nanoplasmonics: Reaching Atomic-Scale Resolution in Nanooptics. *Nano Lett.* **2015**, *15* (5), 3410–3419. https://doi.org/10.1021/acs.nanolett.5b00759.

(35) Trautmann, S.; Aizpurua, J.; Götz, I.; Undisz, A.; Dellith, J.; Schneidewind, H.; Rettenmayr, M.; Deckert, V. A Classical Description of Subnanometer Resolution by Atomic Features in Metallic Structures. *Nanoscale* **2017**, *9* (1), 391–401. https://doi.org/10.1039/C6NR07560F.

(36) Sonnefraud, Y.; Leen Koh, A.; McComb, D. W.; Maier, S. A. Nanoplasmonics: Engineering and Observation of Localized Plasmon Modes. *Laser Photonics Rev.* **2012**, *6* (3), 277–295. https://doi.org/10.1002/lpor.201100027.

(37) Rycenga, M.; Cobley, C. M.; Zeng, J.; Li, W.; Moran, C. H.; Zhang, Q.; Qin, D.; Xia, Y. Controlling the Synthesis and Assembly of Silver Nanostructures for Plasmonic Applications. *Chem. Rev.* **2011**, *111* (6), 3669–3712. https://doi.org/10.1021/cr100275d.

(38) García de Abajo, F. J. Optical Excitations in Electron Microscopy. *Rev. Mod. Phys.* **2010**, *82* (1), 209–275. https://doi.org/10.1103/RevModPhys.82.209.

(39) Colliex, C.; Kociak, M.; Stéphan, O. Electron Energy Loss Spectroscopy Imaging of Surface Plasmons at the Nanometer Scale. *Ultramicroscopy* **2016**, *162*, A1–A24. https://doi.org/10.1016/j.ultramic.2015.11.012.

(40) Huang, T.; Cao, W.; Elsayed-Ali, H. E.; Xu, X.-H. N. High-Throughput Ultrasensitive Characterization of Chemical, Structural and Plasmonic Properties of EBL-Fabricated Single Silver Nanoparticles. *Nanoscale* **2012**, *4* (2), 380–385. https://doi.org/10.1039/C1NR11368B.

(41) Sun, S.; Gao, M.; Lei, G.; Zou, H.; Ma, J.; Huang, C. Visually Monitoring the Etching Process of Gold Nanoparticles by KI/I2 at Single-Nanoparticle Level Using Scattered-Light Dark-Field Microscopic Imaging. *Nano Res.* **2016**, *9* (4), 1125–1134. https://doi.org/10.1007/s12274-016-1007-z.

(42) Itoh, T.; Yamamoto, Y. S.; Suzuki, T.; Kitahama, Y.; Ozaki, Y. Darkfield Microspectroscopy of Nanostructures on Silver Tip-Enhanced Raman Scattering Probes. *Appl. Phys. Lett.* **2016**, *108* (2), 021604. https://doi.org/10.1063/1.4939982.

(43) Movsesyan, A.; Baudrion, A.-L.; Adam, P.-M. Extinction Measurements of Metallic Nanoparticles Arrays as a Way to Explore the Single Nanoparticle Plasmon Resonances. *Opt. Express* **2018**, *26* (5), 6439. https://doi.org/10.1364/OE.26.006439.

(44) Liu, H.; Dong, C.; Huang, X.; Ren, J. Spatially Resolved Scattering Correlation Spectroscopy Using a Total Internal Reflection Configuration. *Anal. Chem.* **2012**, *84* (8), 3561–3567. https://doi.org/10.1021/ac2031833.

(45) Ament, I.; Prasad, J.; Henkel, A.; Schmachtel, S.; Sönnichsen, C. Single Unlabeled Protein Detection on Individual Plasmonic Nanoparticles. *Nano Lett.* **2012**, *12* (2), 1092–1095. https://doi.org/10.1021/nl204496g.

(46) Hoffmann, B.; Vassant, S.; Chen, X.-W.; Götzinger, S.; Sandoghdar, V.; Christiansen, S. Fabrication and Characterization of Plasmonic Nanocone Antennas for Strong Spontaneous Emission Enhancement. *Nanotechnology* **2015**, *26* (40), 404001. https://doi.org/10.1088/0957-4484/26/40/404001.

(47) von Olshausen, P.; Rohrbach, A. Coherent Total Internal Reflection Dark-Field Microscopy: Label-Free Imaging beyond the Diffraction Limit. *Opt. Lett.* **2013**, *38* (20), 4066. https://doi.org/10.1364/OL.38.004066.

(48) Talaga, D.; Comesaña-Hermo, M.; Ravaine, S.; Vallée, R. A. L.; Bonhommeau, S. Colocalized Dark-Field Scattering, Atomic Force and Surface-Enhanced Raman Scattering Microscopic Imaging of Single Gold Nanoparticles. *J. Opt.* **2015**, *17* (11), 114006. https://doi.org/10.1088/2040-8978/17/11/114006.

(49) Yang, J.-H.; Chen, K.-P. Evanescent Wave-Assisted Symmetry Breaking of Gold Dipolar Nanoantennas. *Sci. Rep.* **2016**, *6* (1). https://doi.org/10.1038/srep32194.

(50) Arscott, S. On Evaporation via an Inclined Rotating Circular *Lift-off* Shadow or Stencil Mask. *J. Vac. Sci. Technol. B* **2019**, *37* (1), 011602. https://doi.org/10.1116/1.5057404.

(51) Eschimese, D.; Vaurette, F.; Troadec, D.; Leveque, G.; Melin, T.; Arscott, S. Size and Shape Control of a Variety of Metallic Nanostructures Using Tilted, Rotating Evaporation and

Lithographic Lift-off Techniques. *Sci. Rep.* **2019**, *9* (1). https://doi.org/10.1038/s41598-019-44074-w.

(52) Langhammer, C.; Schwind, M.; Kasemo, B.; Zorić, I. Localized Surface Plasmon Resonances in Aluminum Nanodisks. *Nano Lett.* **2008**, *8* (5), 1461–1471. https://doi.org/10.1021/nl080453i.

(53) Marae-Djouda, J.; Caputo, R.; Mahi, N.; Lévêque, G.; Akjouj, A.; Adam, P.-M.; Maurer, T. Angular Plasmon Response of Gold Nanoparticles Arrays: Approaching the Rayleigh Limit. *Nanophotonics* **2017**, *6* (1), 279–288. https://doi.org/10.1515/nanoph-2016-0112.

(54) Saison-Francioso, O.; Lévêque, G.; Boukherroub, R.; Szunerits, S.; Akjouj, A. Dependence between the Refractive-Index Sensitivity of Metallic Nanoparticles and the Spectral Position of Their Localized Surface Plasmon Band: A Numerical and Analytical Study. *J. Phys. Chem. C* **2015**, *119* (51), 28551–28559. https://doi.org/10.1021/acs.jpcc.5b08357.

(55) Stockman, M. I. Nanofocusing of Optical Energy in Tapered Plasmonic Waveguides. *Phys. Rev. Lett.* **2004**, *93* (13). https://doi.org/10.1103/PhysRevLett.93.137404.

(56) Cui, J.; Yang, L.; Wang, Y. Simulation Study of Near-Field Enhancement on a Laser-Irradiated AFM Metal Probe. *Laser Phys.* **2013**, *23* (7), 076003. https://doi.org/10.1088/1054-660X/23/7/076003.

(57) Geshev, P. I.; Fischer, U.; Fuchs, H. Calculation of Tip Enhanced Raman Scattering Caused by Nanoparticle Plasmons Acting on a Molecule Placed near a Metallic Film. *Phys. Rev. B* **2010**, *81* (12). https://doi.org/10.1103/PhysRevB.81.125441.

(58) Johnson, P. B.; Christy, R. W. Optical Constants of the Noble Metals. *Phys. Rev. B* **1972**, *6* (12), 4370–4379. https://doi.org/10.1103/PhysRevB.6.4370.